# Single Crystal Polarized Spectroscopy of Manganese Superoxide Dismutase and Electronic Structure of the Active Site Metal Complex†

**Mei M. Whittaker,‡ Christopher A. Ekberg,‡ Ross A. Edwards,§ Edward N. Baker,§,|| Geoffrey B. Jameson,§ and James W. Whittaker*,‡**

*Department of Biochemistry and Molecular Biology, Oregon Graduate Institute of Science and Technology, P.O. Box 91000, Portland, Oregon 97291-1000, School of Biological Sciences, University of Auckland, Auckland, New Zealand, and Department of Chemistry and Biochemistry, Protein Structural Laboratory, Massey University, Palmerston North, New Zealand*

*Received: January 14, 1998; In Final Form: April 8, 1998*

Manganese superoxide dismutase from *E. coli* crystallizes from poly(ethylene glycol) solution in the orthorhombic space group $C222_1$. The bladelike purple crystals of the Mn(III) enzyme are strongly pleiochroic in polarized light, appearing red or green for light polarized parallel or perpendicular to their long axis, coincident with the crystallographic *c*-axis. Polarized spectra from oriented single crystals of Mn superoxide dismutase reveal a dramatic dichroism of the optical absorption bands that is primarily associated with a single ligand field transition near 500 nm exhibiting a polarization ratio of greater than 10:1, with amplitude maximizing for polarization parallel to the crystallographic *c*-axis. Detailed analysis of this polarization by projection onto the four Mn sites within the asymmetric unit allows interpretation of the crystal spectra in terms of molecular excitations and active site electronic structure. The strongest polarization is roughly aligned with the carboxylate ligand, suggesting a significant component of carboxylate-to-Mn(III) ligand-to-metal charge-transfer (LMCT) character to this absorption band. Density functional theory calculations on the ground-state electronic structure of an active site model predict strong mixing between the valence levels of the Mn(III) ion and both hydroxide and carboxylate oxyanion donor groups. Furthermore, this indicates that optical polarization in the transition to the second electronic excited state arises from the directional covalency in these metal−ligand interactions. Calculations of geometric and electronic structures of the reduced and protonated Mn(II)($H_2O$) model lead to the prediction that the Mn−O bond stretch coordinate is important for electron-transfer reactivity in the active site. The combination of experimental and computational approaches provides insight into the contributions of endogenous ligands to the electronic structure of the Mn(III) ground state for this important biological redox complex.

## Introduction

Superoxide dismutases are important antioxidant metalloenzymes that serve as survival gear for living cells, providing molecular defense against toxic oxygen metabolites by catalyzing the redox disproportionation of superoxide radical:[1−3]

$$2O_2^{\bullet -} + 2H^+ \rightarrow O_2 + H_2O_2 \qquad (1)$$

Superoxide dismutases are among the fastest known enzymes, approaching the diffusion limit for catalysis.[3] The remarkable effectiveness of these enzymes is in part due to the small (diatomic) substrate and the fact that turnover involves only movement of protons and electrons, making these active sites very efficient one-electron redox engines.

Four classes of superoxide dismutase are now known, distinguished by their metal cofactor (Mn,[4,5] Fe,[6] Cu/Zn,[7] or Ni[8]). Manganese superoxide dismutase occurs cytoplasmically in many bacteria and in the mitochondrial matrix of all eukaryotic cells.[4,5] Crystal structures have been solved for Mn superoxide dismutases from both bacteria (*Thermus thermophilus,*[9] *Escherichia coli*[10]) and eukaryotes (human mitochondria[11]). Prokaryotic and eukaryotic enzymes are highly homologous, allowing near superposition of residues within about 8 Å of the metal ion. In each enzyme, the Mn ion is bound by four protein ligands (three histidine imidazoles and an aspartic carboxylate) and a coordinated solvent molecule (hydroxide or water, depending on the oxidation state of the metal ion) with approximate mirror symmetry for the complex (effective $C_s$ point group for the metal center) (Figure 1).

The structure of the MnSOD active site revealed by crystallography shows the metal center bound in a highly conserved, unique protein environment with well-defined geometry. Like other biological redox systems that have evolved to function as rapid electron-transfer agents including cupredoxins, iron−sulfur proteins, and cytochromes,[12,13] the active site structure is virtually identical in oxidized and reduced states, implying a relatively small reorganization barrier for redox. However, the MnSOD site is distinct from simple electron-transfer complexes in that it exhibits coordination chemistry,[14,15] binding small anions at the Mn center, and its redox transformations are coupled to proton equilibria in the active site.[16] These aspects of redox reactivity, ligand affinity, and proton coupling relate directly to the electronic structural features of the complex and

* Corresponding author: telephone 503-690-1065; FAX 503-690-1464; E-mail jim@insight.cbs.ogi.edu.

† Support for this project from the National Institutes of Health (GM 42680 to J.W.W.) is gratefully acknowledged.

‡ Oregon Graduate Institute of Science and Technology.
§ Massey University.
|| University of Auckland.

S1089-5647(98)00775-5 CCC: $15.00 
Published on Web 05/19/1998

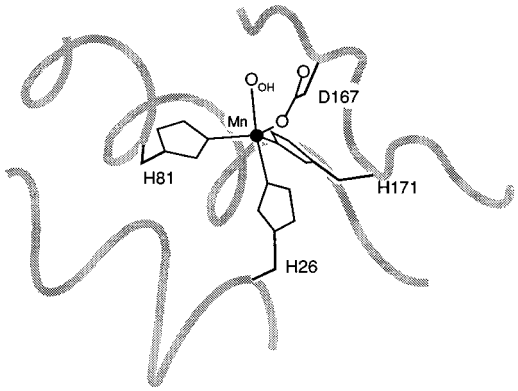


**Figure 1.** Active site structure of Mn superoxide dismutase (based on a 2.1 Å resolution crystal structure for *E. coli* Mn superoxide dismutase (ref 10)).

lie beyond the atomic resolution provided by protein crystallography, at a level of electronic structural detail requiring an extension by spectroscopic and computational methods.

Previous spectroscopic characterization of the Mn(III) active site of superoxide dismutase by optical absorption,[14,15,17] circular dichroism (CD),[14,15,17] and magnetic circular dichroism (MCD)[14] spectroscopies has provided basic information on the metal ion and its ligand interactions. Optical spectra for the active site Mn(III) ion have resolved the four spin-allowed ligand field transitions for the high-spin $d^4$ metal center in the protein. Comparison with data for Mn(III) inorganic model complexes allows the spectra to be interpreted in terms of a rhombically perturbed low-symmetry five-coordinate metal center[14,15] and has revealed important features of coordination chemistry and dynamics in the active site complex.[15,18] Recent theoretical studies have begun to investigate the electronic ground state of the active site complex to explore the role of electronic structure in active site properties.[19]

Still, key questions on the nature of the Mn(III) ground state and the role of metal ligands in the electronic properties of the active site metal ion have yet to be clearly answered. The role of ligand covalency in stabilizing the Mn(III) complex and identification of the basic features of electronic structure important for redox and proton coupling are of special interest in terms of the catalytic chemistry of the active site complex. We report here the results of a combination of experimental and computational approaches to explore the information contained in the optical spectra of the Mn(III) containing *E. coli* MnSOD. Polarized spectra for oriented MnSOD molecules in a single crystal have given directional resolution of the absorption bands, allowing assignment of intensity to specific ligand interactions based on the crystallographic data. Computational studies complementing these experiments and calibrated by the spectroscopic results provide a deeper insight into the nature of the electronic ground state relating to interactions between the Mn(III) ion and its protein environment. Together these investigations develop a clearer picture of the electronic factors important for the catalytic function of this biological metal complex.

## Materials and Methods

An *E. coli* strain (AB2463/pDT1-5) containing a MnSOD expression plasmid bearing the *E. coli sodA* structural gene[20] was a generous gift from Dr. Danièle Touati (Institut Jacques Monod, Centre National de la Récherche Scientifique, Université Paris VII). Cultures were grown in 2× Luria-Bertani (LB) media supplemented with 1% glucose, 120 $\mu$g/mL ampicillin, and 30 $\mu$M Mn(II). Further additions of ampicillin (150 mg/L) were made hourly after the optical density reached 0.3 at 600 nm, and a second addition of 1% glucose was made at mid log phase. Fermentations for protein preparation were routinely performed in a 10 L New Brunswick Scientific BioFlo 3000 bioreactor at 37 °C with vigorous agitation and $O_2$ purging. Superoxide dismutase was purified as previously described[14] with an additional chromatofocusing chromatography step using PBE-94 polybuffer exchanger and Polybuffer-74 ampholyte. Superoxide dismutase activity was measured using the xanthine oxidase/cytochrome *c* inhibition assay.[7] Mn superoxide dismutase was crystallized using a modification of the previously described procedure.[10,21]

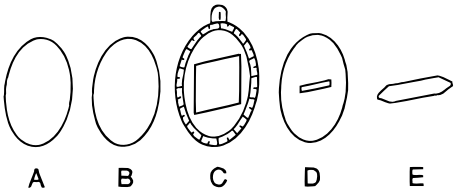


**Figure 2.** Polarization optics for measuring crystal spectra: (A, B) Tandem quartz wedge depolarizers in quadrature, (C) Glan-Thompson polarizing prism in goniometer mount, (D) optical mask, (E) MnSOD crystal.

Protein concentration was routinely determined by the method of Lowry[22] and by optical absorption measurements using the previously reported molar extinction coefficient ($\epsilon_{280} = 8.66 \times 10^4$ $M^{-1}$ $cm^{-1}$).[23] Metal quantitation was performed by atomic absorption spectrometric analysis using a Varian SpectrAA 20B atomic absorption spectrometer equipped with a GTA-96 graphic furnace for high-sensitivity analytical determinations. All reagents for preparation of culture media and buffers were from commercial sources and were used without purification. Ampicillin was obtained from Sigma Chemical Co.

The morphology of the *E. coli* MnSOD crystals was determined by indexing diffraction patterns recorded on a Rigaku Raxis IIC image-plate area detector. The needle axis was aligned perpendicular to the beam, and patterns were recorded with the incident beam perpendicular to the faces defining the needle. The *c*-axis was identified as the needle axis, and the well-developed faces as were identified as {100} and {010}. The red or green pleiochroism was confirmed for light polarized respectively parallel or perpendicular to the needle axis previously identified unequivocally as the crystallographic *c*-axis by diffraction experiments on the same crystal as described above. The morphological assignment was confirmed on several crystals.

Optical absorption spectra were recorded on a Varian Cary5 UV−vis−NIR absorption spectrometer interfaced with a PC for data acquisition. Polarized absorption data were obtained using the optics illustrated in Figure 2. Tandem quartz wedge depolarizers (Harrick Scientific Corp., Ossining, NY) were required to remove the partial polarization of light exiting the dual grating/prism monochromator, with quadrature orientation for the wedge axes to maximize efficiency of polarization scrambling. A 1 cm Glan-Thompson polarizing prism (*f*/0.4) (Harrick Scientific Corp., Ossining, NY) in a goniometer mount provided nearly achromatic linear polarization over the visible−near-infrared spectral range. Stray light was masked around the protein crystal by a slit aperture cut in 0.1 mm thick Cu sheet metal. The protein crystal was mounted in a 1 mm path length quartz cuvette in crystallization mother liquor.

Electronic structure calculations were performed using self-consistent density functional (DF) methods implemented in the program DMol (Biosym Technologies, San Diego). DMol uses

the Heden−Lundquist/Janak−Morruzi−Williams[24] local correlation functional with Becke 88[25] exchange and Perdew−Wang (PW)[26] correlation nonlocal corrections, providing first principles calculation of electronic structures of molecular systems. For large (many-electron) systems, DF methods offer significant advantages in computational efficiency over Hartree−Fock calculations. The calculations were performed using a double numeric basis extending to the third harmonics for all non-hydrogen atoms which allows for adequate treatment of polarization effects. Molecular geometry optimization was performed by relaxing the structure in a spin-unrestricted, correlated ab initio potential with perturbative treatment of nonlocal corrections to the energy. During geometry optimization, significant eigenvector mixing was allowed to accelerate convergence[27,28] while stricter convergence criteria ($\leq$0.05 mixing coefficients for electron density and spin) were used to obtain high-quality ground-state wave functions. Inner core eigenvectors were frozen on carbon, nitrogen, oxygen, and manganese atoms leaving 63 $\alpha$ and 59 $\beta$ active valence electrons in the calculation (for a total of 122 active electrons for the Mn(III) complex). Calculations were performed on a Silicon Graphics Power Indigo$^2$ XZ workstation with a R8000 processor running under the 64-bit Irix 6.2 operating system. Graphical displays were printed from the InsightII molecular modeling interface (Biosym Technologies, San Diego).

### Spectroscopic Results

*E. coli* MnSOD crystallizes from poly(ethylene glycol) solution as large blades (Figure 3) in the orthorhombic space group $C222_1$.[10] The crystal morphology reflects the twofold symmetries of the lattice, and X-ray analysis indicates that the crystallographic *c*-axis is aligned with the needle axis of the crystals. The crystals are pleiochroic, appearing red or green in light polarized parallel or perpendicular to the crystallographic *c*-axis, respectively. The largest well-developed face in this prismatic habit is assigned as the lattice plane with Miller indices (010) based on X-ray morphological analysis. The asymmetric unit in this lattice contains two MnSOD dimers (four metal centers) with orientations shown in Figure 3. The twofold rotations of the lattice symmetry applied to the asymmetric unit leave the magnitude of the projections of the metal−ligand (M−L) vectors on the crystal axes unchanged over the 32 Mn sites in the unit cell.

A large, well-formed single crystal (8.2 × 1.3 × 0.9 mm linear dimensions) of orthorhombic MnSOD was chosen for optical absorption measurements. Orthorhombic crystals are optically biaxial, the three mutually perpendicular principal optical directions coinciding with the three orthogonal crystal axes (*a*, *b*, *c*) for all wavelengths.[29] In orthorhombic space symmetry, the extinction directions (directions along which light propagates without change in polarization) lie parallel to crystallographic directions. Extinction for light polarized parallel and perpendicular to the long axis of the crystal was confirmed by inspection of the crystal between crossed polarizers. The crystal was mounted in a quartz cell masked by a slit slightly smaller than the crystal to avoid light leaks that reduce polarization intensities.[30] Absorption measurements were performed with light at normal incidence to the (010) crystal face having polarization parallel or perpendicular to the crystallographic *c*-axis. Independent measurements with the crystal removed from the optic path confirmed the polarization independence of the spectral baseline.

Absorption spectra of an oriented crystal are dramatically different for light polarized parallel (Figure 4, above) or perpendicular (Figure 4, below) to the crystallographic *c*-axis. In perpendicular polarization, absorption maxima are recorded at 462 and 600 nm with a shoulder at 422 nm and a well-defined absorption minimum at 549 nm, whereas in parallel polarization, the absorption maximum occurs at 513 nm with nearly twice the maximum intensity observed in perpendicular polarization. The two spectra are therefore approximately complementary in intensity across the visible spectrum. Gaussian deconvolution of these spectra over the energy domain based on the transition energies previously determined by a combined absorption, CD, and MCD measurements on the native Mn(III) protein[14,15] resolves the individual ligand field transitions contributing to the broad visible absorption envelope (Figure 4). The results of this analysis are given in Table 1, including the experimental polarization ratios ($A_{\parallel}/A_{\perp}$) for each of the resolved ligand field bands. Three of the absorption bands exhibit only minor

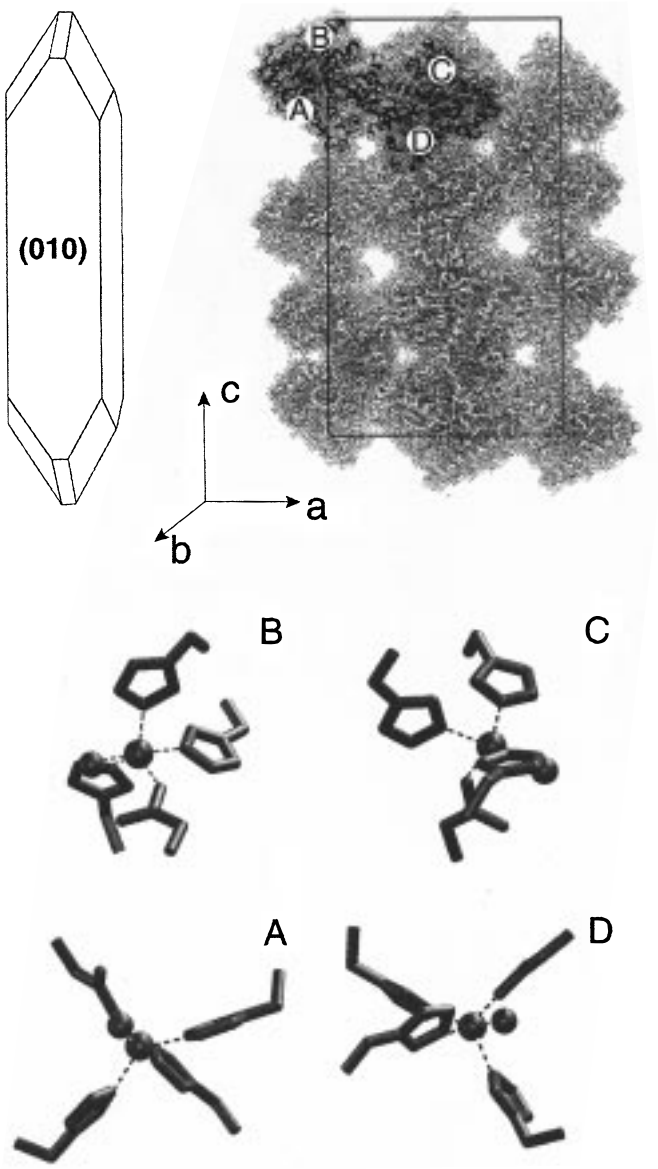


**Figure 3.** (top) Crystal morphology and unit cell structure for *E. coli* MnSOD based on the crystallographic coordinates (from ref 10). (bottom) Projection of each of the four unique sites onto the *ac* crystallographic plane. The four unique active site complexes (A, B, C, D) of the crystallographic asymmetric unit are shown in projection with the crystallographic axis system (insert). The orientation of the Mn−carboxylate vector is predominantly along the crystallographic *c* direction.

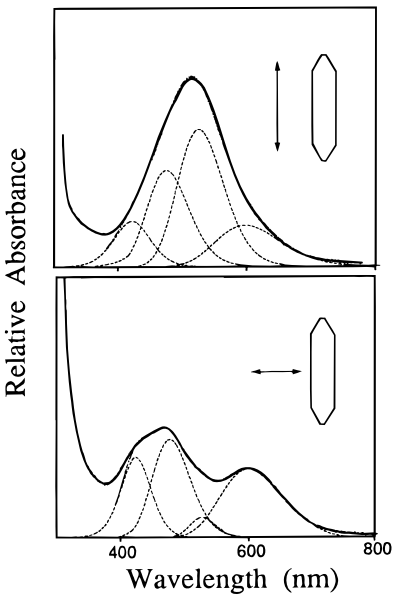


**Figure 4.** Gaussian deconvolution of oriented crystal spectra: (- - -) individual Gaussian components; (···) sum of Gaussian components; (—) experimental spectra. (top) Parallel polarization, (bottom) perpendicular polarization.

**TABLE 1: Gaussian Deconvolution of Polarized Crystal Absorption Spectra for Mn Superoxide Dismutase**

| | | parallel polarization | | perpendicular polarization | | |
|---|---|---|---|---|---|---|
| absorption band | energy ($cm^{-1}$) | int ($A_{rel}$) | Γ ($cm^{-1}$) | int ($A_{rel}$) | Γ ($cm^{-1}$) | polarization ratio ($A_{\|}/A_{\perp}$) |
| 1 | 16 720 | 0.325 | 3295 | 0.524 | 3170 | 0.65 |
| 2 | 19 025 | 1.065 | 3044 | 0.149 | 1760 | 12.3 |
| 3 | 21 040 | 0.748 | 3400 | 0.676 | 3010 | 1.25 |
| 4 | 23 700 | 0.358 | 3500 | 0.644 | 3585 | 0.54 |

polarization, while the fourth (near 19025 $cm^{-1}$, 525 nm) has more than 12-fold higher polarization along the *c*-axis.

## Computational Results

An idealized $C_s$ symmetric model for the active site of Mn superoxide dismutase that retains the essential features of the protein structure while eliminating details that complicate interpretation is shown in Figure 5 (above). The model approximates histidine ligands as imidazoles and replaces the aspartate ligand by acetate and simplifies the geometry by raising the molecular symmetry from $C_1$ to $C_s$. Each of these changes directs attention to key aspects of the active site structure and at the same time improves computational efficiency. Symmetrization of the structure was achieved by a slight rotation of the axial imidazole of histidine H26 and the carboxylate of aspartate D167 into a plane passing through the metal ion and the two ligating atoms and reflection of the coordinating imidazole of histidine H81 across this plane to generate a symmetric complementary equatorial imidazole ligand. In preliminary calculations, solving the electronic ground state of an active site Mn(III) model using the crystallographic M−L distances led to the appearance of low-lying levels of ligand character implying ligand-centered redox in the complex, indicating that geometry optimization is required to obtain a physically realistic ground-state electronic structure. Using the crystallographic distances as the starting point, the idealized structure was relaxed in spin-unrestricted ab initio potentials (with correlation and exchange corrections treated perturbatively) to optimize geometry within the $C_s$ point symmetry constraint. The major change resulting from this optimization step is a significant shortening of the Mn−OH bond distance in the relaxed, optimized geometry (1.77 Å) compared to the crystal structure (2.18 Å).[10] Experimental Mn−O bond distances from other MnSOD structures (*Thermus* MnSOD, 2.06 Å;[9] human MnSOD, 2.06 Å[11]), while shorter than that found for *E. coli* MnSOD, are still longer than the calculated value. The optimized structure retains the roughly trigonal geometry of the protein complex and preserves a hydrogen-bonding interaction between the hydroxide ligand ($HO^-$) and the noncoordinating carboxylate oxygen inferred from the crystal structure. The difference between experimental (crystallographic)[9−11] and theoretical structures may in part be due to the fact that the geometry optimization is performed in vacuo rather than in a protein/solvent dielectric but may also represent a refinement of the crystallographic model building which tends to be relatively imprecise for single-atom nonprotein components. In general, very high-resolution data are required to accurately define M−L distances in metalloprotein crystallography. The discrepancy between experimental and calculated Mn−O distances may also reflect heterogeneity in the metal oxidation state in the protein crystals. (Supporting this view, a Mn(III)−OH bond distance ($d_{Mn-O}$ = 1.827 Å) only slightly different from the computed value has recently been reported for a trigonal-bipyramidal inorganic complex.[31]) In any case, the close similarity between crystallographic and optimized structures suggests that the protein does not significantly constrain the geometry of the complex.

The ground-state electronic structure was solved for this active site model at the double numeric level of spin-unrestricted density functional theory (DFT) as described in the Methods section to obtain estimates of the valence level wave functions for the complex. Under the $C_s$ point group symmetry of the complex, molecular orbitals are either symmetric (a′) or antisymmetric (a″) with respect to the $\sigma_h$ molecular mirror plane, and atomic orbitals composing each molecular orbital must conform to this symmetry. Transformation properties of metal d-orbitals and of valence p-orbitals of hydroxide and carboxylate ligand O atoms that are most important for the valence structure of this complex are given in Table 2.

Isosurface contours for the five highest-lying molecular orbitals spanning the Fermi level are shown in Figure 6. The lowest vacant orbital (at −6.1 eV binding energy, a′ symmetry) is a linear combination of $d_{x^2-y^2}$ and $d_{z^2}$ in the $C_s$ framework, with the *z*-axis perpendicular to the symmetry plane. The equivalent description in terms of the more conventional pseudotrigonal axis system (having the molecular *z*-axis along the Mn−OH direction) is obtained by applying an active rotation through an Euler angle $\gamma = \pi/2$ to this wave function and projecting the transformed function onto the new basis set. In the pseudotrigonal axis system the lowest-lying vacant orbital is nearly pure $d_{z^2}$ character (Table 3) consistent with the dominant trigonal perturbation of the equatorial ligand set. The group of five highest-lying molecular orbitals are all of predominantly metal character (Table 3) with an average metal content of 61%. The reduction from pure metal character is a consequence of covalency in the M−L interactions, as shown by the substantial hydroxide and carboxylate contributions to the valence wave functions (Table 3). These interactions may be defined as $\pi$ or $\sigma$ or depending on whether a nodal plan lies along the M−L axis. The $\sigma$-bonding interactions of both hydroxide (HO) and carboxylate (COO) groups with the Mn ion are associated with orbitals of a′ character while $\pi$

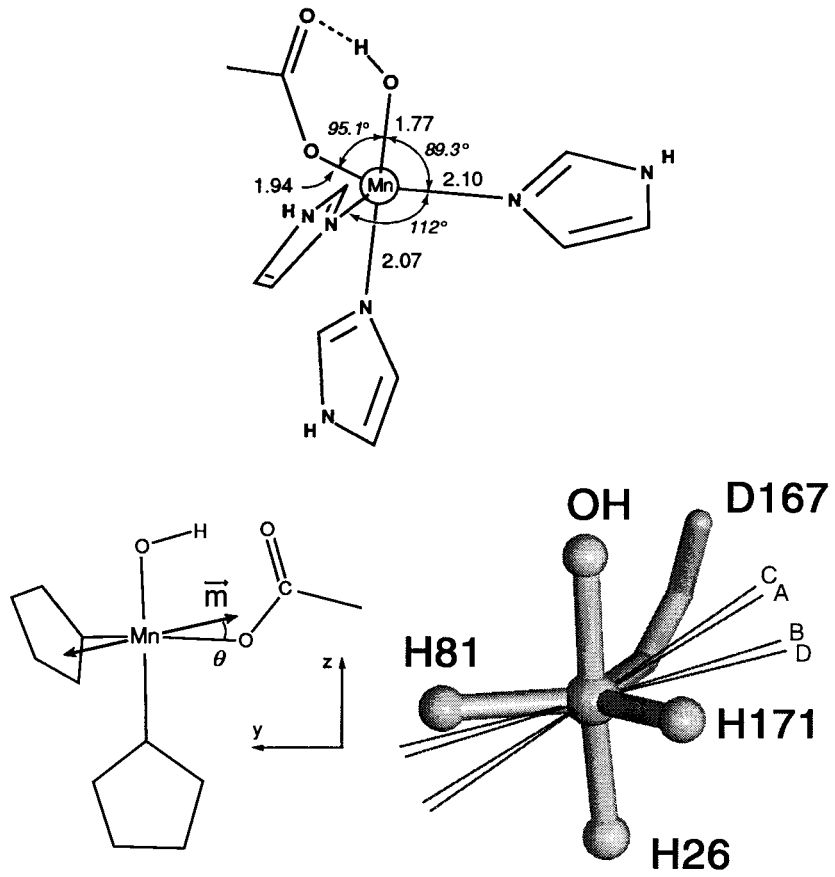


**Figure 5.** Idealized Mn(III)(OH) active site model for calculations of electronic structure. (above) The molecular structure was optimized by relaxing the $C_s$-symmetrized crystallographic geometry in a spin-unrestricted ab initio potential with correlation and exchange computed by DMol DFT within the local density approximation. Bond distances in angstroms. (below, left) Polarization of ligand field excitation projected onto the molecular framework. The electric dipole transition moment vector (**m**) computed for the second spin-allowed ligand field transition ($\Gamma_0 \rightarrow \Gamma_2$ in Table 4) is superimposed on the active site model. The angle between the dipole transition vector and the Mn−O(carboxylate) bond vector ($\theta$) is approximately 13°. (below, right) Projection of the crystallographic *c*-axis (the dominant polarization direction for the crystal spectra) in the local molecular frames of the four unique complexes of the asymmetric unit. The complexes have been superimposed to indicate the degree of alignment.

**TABLE 2: Classification of Atomic Orbitals in the $C_s$ MnSOD Model**

| symmetry | Mn 3d[a] | O 2p |
|---|---|---|
| A′ | $x^2 - y^2$, $z^2$, $yz$ | $y$, $z$ |
| A″ | $xz$, $xy$ | $x$ |

[a] Metal and ligand orbitals are consistently defined in the pseudo-trigonal axis system (*z* along the Mn−OH direction) rather than the $C_s$ axis system.

interactions involve both a′ ($\pi_y$) and a″ ($\pi_x$) symmetry orbitals. These two oxygen-donor ligands dominate the covalent perturbation of the Mn(III) ion, consistent with well-established Mn−oxygen affinities.

Metal−ligand interactions are exclusively antibonding in character over these orbitals, as illustrated by the change in phase that occurs in each wave function between the metal and ligand components (Figure 6). This interaction destabilizes the set of metal-centered orbitals, which lie nearly l eV above the closest ligand-centered orbital. The majority of ligand contributions alternate between hydroxide and carboxylate over this set of orbitals. The LUMO ($\phi_0$, a′ symmetry (Table 3)) is the redox orbital in the complex. This MO has significant $\sigma$-OH antibonding character, associated with the effective $\sigma$ overlap of the $d_{z^2}$ metal orbital with axial ligands. Orbital $\phi_1$ (a″ symmetry) exhibits substantial $\pi_x$-OH mixing, orbital $\phi_2$ (a′ symmetry) has predominantly $\sigma$-COO mixing with lesser $\pi_y$-OH character, orbital $\phi_3$ (a″ symmetry) involves admixture of $\pi_x$-OH plus some $\pi$-COO character, and orbital $\phi_4$ (a′ symmetry) has ligand contributions from both $\pi_y$-OH and $\sigma$-COO. Contributions of the carboxylate ligand include orbitals on both ligated and nonligated oxygens, so the entire carboxylate group is important for the properties of this complex. This analysis indicates a significant degree of ground-state charge transfer from the coordinated groups, nearly equally divided between the hydroxide and carboxylate over the four occupied metal valence MOs.

Light absorption leads to electronic excitation of this complex from the ground-state configuration $\Gamma_0$ ($\phi_0^0\phi_1^1\phi_2^1\phi_3^1\phi_4^1$), forming a series of low-lying ligand field excited states differing from the ground state in the identity of the unoccupied orbital associated with the hole in the metal valence shell. Many-electron orbital states are defined by the hole wave function in a high-spin $d^4$ metal complex, leading in this case to a $^5$A′ many-electron molecular ground term for the Mn(III) ion. One-electron excitations principally involve a change in occupancy of the hole function and a second singly occupied metal orbital which labels the excited state. The overall displacement of electronic charge is a consequence of the spatial distribution of orbital amplitudes for these two wave functions determining the orientation and magnitude of the transition dipole moment vector. The relation between orbital, state, and configuration descriptions is summarized in Scheme 1.

The orientation of the transition dipole vector calculated for the second ligand field excitation ($\Gamma_0 \rightarrow \Gamma_2$, 1A′ → 2A′) (Figure

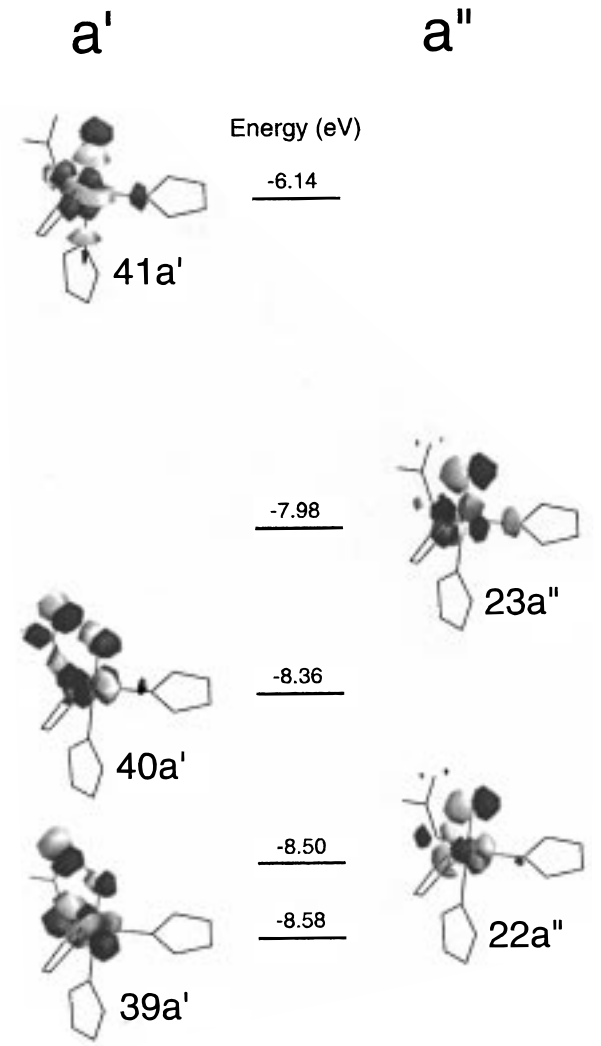


**Figure 6.** Valence molecular orbitals for the Mn(III) active site model. Isosurface representations contoured at 0.05 e/Å$^3$ shaded to indicate relative phase for wave functions solved by DMol DFT. Energies for these molecular eigenvectors are shown on the bars.

5, lower left) reflects the spectroscopic consequences of the carboxylate interactions described above. In this case the change in orbital wave function between ground and excited configurations indicates a large carboxylate-to-Mn(III) ligand-to-metal charge-transfer (LMCT) contribution to intensity in this transition. While LMCT transition dipoles are normally aligned with M−L bond vectors for the directly coordinating atoms (see below), the transition moment calculated for this transition is tilted away from the Mn−O(carboxylate) direction by approximately 13° toward the second, nonligating oxygen. This tilt reflects significant contributions of this second oxygen to charge displacement in this transition. More generally, the contributions of the hydroxide ligand in ground and excited states can be expected to be an additional factor determining the orientation of the transition dipole. The ground-state covalent mixing of ligand wave functions is thus expressed in the intensity and polarization of the excited-state spectra.

The transition energies for one-electron excitations of the complex can be estimated directly from orbital splitting energies in the ground state ($\Delta E_{opt} \approx \Delta E_{orb}$), assuming that the orbital energies are the same in the initial- and final-state configurations. However, this estimate can often be improved by applying Slater transition-state theory, in which the energies are calculated for an electronic configuration representing the midpoint of the excitation.[32] Excitation in a localized system involves changes in eigenvalues through the dependence of the interelectron potential (used in constructing the density) on eigenvector occupation numbers. This leads to a dependence of the self-consistent energies on occupation numbers that can be taken into account by performing a calculation in the same geometry with half-integral occupation of the two orbital eigenvectors involved in the transition. Slater transition-state theory applied to the MnSOD model gives the magnitude of the correction to the computed transition energies, the energy of the lowest excitation ($\Gamma_0 \rightarrow \Gamma_1$, $1A' \rightarrow 1A''$) being 14 872 cm$^{-1}$ (uncorrected) and 16 455 cm$^{-1}$ (corrected). This same scaling correction applied to the other ligand field transitions leads to predicted transition energies (16 455, 19 783, 21 088, and 21 805 cm$^{-1}$) for the four spin-allowed transitions of the Mn(III) metal ion in this complex for comparison with experimental values for *E. coli* MnSOD (16 720, 19 025, 21 040, and 23 700 cm$^{-1}$).[15]

The DFT calculations were extended to investigate the effect of stepwise one-electron reduction and protonation on the active site model:

$$\underset{\mathbf{A}}{\text{Mn(III)(OH)}} \xrightarrow{e^-} \underset{\mathbf{B}}{\text{Mn(II)(OH)}} \xrightarrow{H^+} \underset{\mathbf{C}}{\text{Mn(II)(H}_2\text{O)}} \qquad (2)$$

$C_s$ symmetry was preserved in the Mn(II)(OH) complex (**B**), while protonation lowered the molecular symmetry to $C_1$ for the Mn(II)($H_2O$) aquo complex (**C**). During geometry optimization of the reduced Mn(II) complexes the search was restricted to the high-spin ($S = {}^5/_2$) potential surface by requiring the five highest-lying MOs to be occupied by electrons with α spin. The one-electron reduced complex **B** retained the basic structure shown in Figure 5, with an average expansion of 8% in the M−L bond distances. The largest increases occurred in the Mn−OH distance (from 1.77 to 1.97 Å) and in the Mn−N distance for the axially coordinated imidazole (from 2.07 to 2.28 Å). The covalency of the M−L interactions was correspondingly less in the reduced complex, as reflected in the increase in M 3d character of the valence wave functions from an average of 64% in the Mn(III) ground state to 67% in the Mn(II) ground state (Table 4). A decrease in the covalency of Mn interactions with the hydroxide and carboxylate ligands accounts for the majority of this change. The structure of complex **C** is further perturbed by protonation of the solvent, leading to an additional stretch in the Mn−O bond distance (to 2.14 Å) and a twist of the imidazole ring proximal to the protonation site to accommodate the solvent hydrogen (Figure 7). Mn covalency is lower still in this complex, with valence M 3d character increasing to 73% over the five highest-lying MOs in the valence shell, principally the result of the stabilization of the solvent oxygen orbitals by addition of the proton (Table 5).

## Discussion

Of all the reactions that occur in biochemistry, simple redox chemistry performed by a metalloenzyme active site is most directly related to electronic structure. Redox reactions essentially imply a change in electron configuration that can be described as a charge-transfer (CT) process involving specific orbitals in the complex. The link between electronic structure and reactivity can be expected to be relatively direct for metalloenzymes because the small number of valence orbitals involved in chemistry are more or less localized on the coordinated metal ion.

Electron transfer in biology is often associated with small metalloprotein complexes (cupredoxins, iron−sulfur proteins,

**TABLE 3: Orbital Decomposition of Valence Wave Functions for the Mn(III)(OH) Active Site Model[a]**

| molecular orbital | $d_{x^2-y^2}$ | $d_{xz}$ | $d_{z^2}$ | $d_{yz}$ | $d_{xy}$ | $\sum c_{M3d}^2$ | $\sum c_{OH}^2$ | $\sum c_{COO}^2$ |
|---|---|---|---|---|---|---|---|---|
| 0 (41a′) | 0.1031 | 0.0007 | 0.7848 | −0.0336 | 0.0001 | 0.63 | 0.24 | 0.12 |
| 1 (23a″) | 0.0002 | 0.6595 | −0.0001 | 0.0034 | −0.4613 | 0.65 | 0.31 | 0.07 |
| 2 (40a′) | 0.6135 | 0.0265 | −0.1338 | −0.4066 | 0.0180 | 0.56 | 0.16 | 0.27 |
| 3 (22a″) | −0.0222 | 0.5722 | 0.1729 | 0.0000 | 0.5792 | 0.69 | 0.23 | 0.09 |
| 4 (39a′) | 0.5314 | 0.0044 | −0.0377 | 0.4782 | 0.0154 | 0.51 | 0.08 | 0.41 |

[a] Metal 3d orbital coefficients ($c_{M3d}$) from DFT numerical wave functions solved in $C_s$ site symmetry (*z*-axis perpendicular to symmetry plane) were transformed to an axis system having the molecular *z*-axis aligned with the pseudotrigonal axis of the complex for clarity as described in the text.

**SCHEME 1**

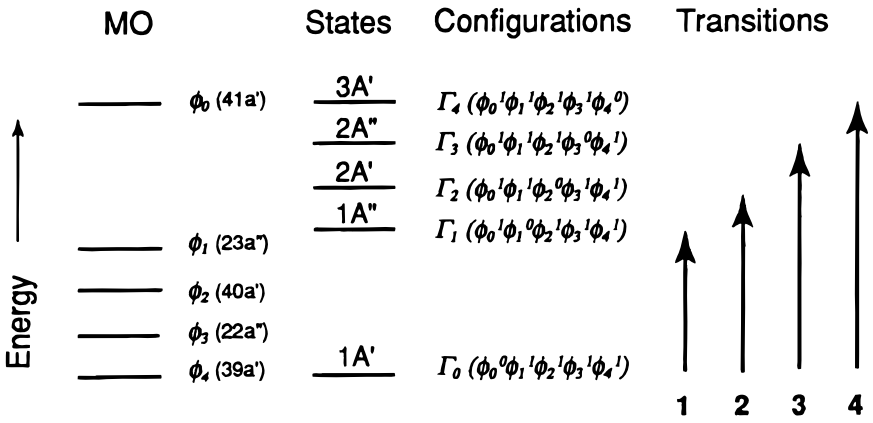


**TABLE 4: Orbital Decomposition of Valence Wave Functions for the Mn(II)(OH) Active Site Model[a]**

| molecular orbital | $d_{x^2-y^2}$ | $d_{xz}$ | $d_{z^2}$ | $d_{yz}$ | $d_{xy}$ | $\sum c_{M3d}^2$ | $\sum c_{OH}^2$ | $\sum c_{COO}^2$ |
|---|---|---|---|---|---|---|---|---|
| 0 (41a′) | 0.1525 | 0.0000 | 0.8413 | 0.0804 | 0.0000 | 0.74 | 0.20 | 0.10 |
| 1 (23a″) | 0.0000 | 0.3997 | 0.0000 | 0.0000 | 0.6622 | 0.60 | 0.39 | 0.01 |
| 2 (22a″) | 0.0000 | −0.8090 | 0.0000 | 0.0000 | −0.2911 | 0.74 | 0.09 | 0.12 |
| 3 (40a′) | 0.5649 | 0.0000 | −0.0726 | −0.6502 | 0.0000 | 0.75 | 0.07 | 0.12 |
| 4 (39a′) | −0.5962 | 0.0000 | 0.1388 | −0.4020 | 0.0000 | 0.54 | 0.04 | 0.29 |

[a] Metal 3d orbital coefficients ($c_{M3d}$) from DFT numerical wave functions solved in $C_s$ site symmetry (*z*-axis perpendicular to symmetry plane) were transformed to an axis system having the molecular *z*-axis aligned with the pseudotrigonal axis of the complex for clarity as described in the text.

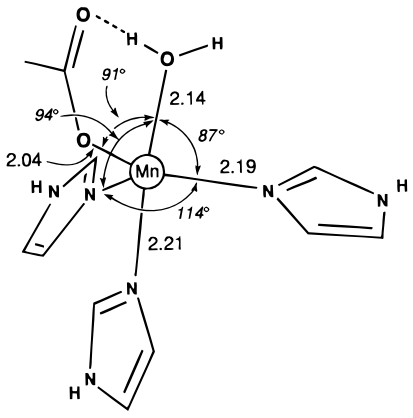


**Figure 7.** Idealized Mn(II)($H_2O$) active site model for calculations of electronic structure. The molecular structure was optimized by relaxing geometry in a spin-unrestricted ab initio high-spin ($S = {}^5/_2$) potential with correlation and exchange computed by DMol DFT within the local density approximation. Bond distances in angstroms.

or cytochromes)[12,13] in which copper or iron metal ions store electrons carried in intracellular redox circuits without change in coordination of the redox-active metal ion. Redox chemistry is also important in a wide range of catalytic reactions (including oxygen and nitrogen activation) performed by redox sites that have labile structures able to bind and activate small molecules. Mn superoxide dismutase contains a catalytic metal center that is in many ways similar to the cupredoxin and FeS proteins in terms of very limited rearrangements associated with metal redox, but MnSOD exhibits coordination chemistry and its redox reaction is coupled to proton transfer as part of its catalytic function. Since electronic processes are essential to the function of the MnSOD complex, its electronic structure is especially interesting. This level of electronic structural detail can be reached experimentally using spectroscopic methods, which provide information on electronic wave functions (molecular orbitals) and interactions in intensity, polarization, and energy splittings.

The electronic ground state of the high-spin Mn(III) ion in MnSOD, defined by the hole in the metal valence shell, is found in the all-valence electron DFT calculation to be a linear combination of metal d-orbitals ($d_{x^2-y^2}$ and $d_{z^2}$), corresponding to nearly pure $d_{z^2}$ under axis rotation to make the pseudotrigonal axis of the complex (along the Mn−OH vector) the *z*-axis. In $C_s$ site symmetry all levels are nondegenerate, consistent with the experimentally determined resolution of all four spin-allowed ligand field transitions for the high-spin Mn(III) ion in the protein. The theoretical ground state is thus predominantly $d_{z^2}$ character mixed with ligand wave functions through covalency, essentially the same as previously predicted qualitatively on the basis of ligand field theory. In addition, the present calculation provides estimates of ligand covalency terms that are important for the stabilization of metal redox states. These terms also give rise to intensity in optical spectra, allowing spectroscopic

**TABLE 5: Orbital Decomposition of Valence Wave Functions for the Mn(II)($H_2O$) SOD Active Site Model**[a]

| molecular orbital | $d_{x^2-y^2}$ | $d_{xz}$ | $d_{z^2}$ | $d_{yz}$ | $d_{xy}$ | $\sum c_{M3d}^2$ | $\sum c_{OH}^2$ | $\sum c_{COO}^2$ |
|---|---|---|---|---|---|---|---|---|
| 0 (64a) | −0.1296 | 0.1300 | −0.8761 | 0.1281 | 0.0547 | 0.82 | 0.16 | 0.09 |
| 1 (63a) | −0.2893 | 0.7964 | 0.1882 | −0.0251 | −0.0712 | 0.76 | 0.01 | 0.14 |
| 2 (62a) | 0.7448 | 0.3373 | −0.1012 | 0.1687 | −0.0438 | 0.71 | 0.00 | 0.19 |
| 3 (61a) | −0.1856 | −0.0576 | 0.1025 | 0.6808 | 0.0340 | 0.51 | 0.15 | 0.40 |
| 4 (60a) | −0.0361 | −0.0794 | −0.0813 | 0.0241 | −0.9210 | 0.86 | 0.05 | 0.01 |

[a] Metal 3d orbital coefficients ($c_{M3d}$) from DFT numerical wave functions solved in $C_1$ site symmetry (with the *z*-axis aligned as described for the $C_s$ complexes) were transformed to an axis system having the molecular *z*-axis aligned with the pseudotrigonal axis of the complex for clarity as described in the text.

measurements (energies and polarizations) to check and calibrate theoretical results.

The origin of intensity in these spectra can be somewhat problematic. Although the lowest-lying spectroscopic transitions of metal complexes are conventionally described as ligand field transitions, pure d → d excitation is strictly forbidden by Laporte orbital selection rules for electric dipole absorption.[33,34] Any intensity in these spectra thus arises from intensity borrowing via admixture of odd parity wave functions through the combination of covalency and low symmetry. Covalency gives electric dipole allowed charge-transfer character to an electronic transition that consequently acquires polarization from the directional character of orbital mixing. The transition dipole moment for LMCT is aligned with the charge translation axis which for a simple monatomic ligand corresponds to the M−L bond vector.[30]

Electric dipole allowed transitions are excited by translation of electronic charge defining a transition moment vector (**m**; $m_i = x,y,z$) that can be computed from the theoretical wave functions. The amplitude for polarized absorption depends on the projection of this transition dipole vector onto the electric field vector of light. Dipole moments for LMCT transitions of simple ligands (e.g., halides) are aligned along the M−L bond vector. In an oriented sample such as a single crystal with lower than cubic symmetry, polarized light excites only molecules having a nonzero component of their transition dipole moment projecting in a plane containing the radiation electric field **E** perpendicular to the propagation direction of the light. In general, the molecular and lattice frames are not aligned, and multiple copies of the molecule may occur within the asymmetric unit with distinct orientations. Each of these copies will contribute to the total polarized absorption based on projection of **E** within the local molecular frame. An overall alignment of local molecular axes over the lattice is necessary to give significant polarization to the absorption spectra. Within the asymmetric unit of the *E. coli* MnSOD crystal (Figure 3), the active sites are roughly oriented with the carboxylate ligands lying approximately along the crystallographic *c*-axis.

The sum over polarizations for light propagating parallel to each of the three crystal axes having polarization aligned with the two perpendicular axes (in principle) composes a rotationally averaged optical spectrum allowing comparison with solution data. The contribution of oriented absorption to the averaged spectrum is given by

$$\sum_q \sum_p A_{q,p} = A_{\text{rot avg}} \tag{3}$$

where the sums are over the propagation vector ($q = a,b,c$ (the orthorhombic crystal axes)) and polarizations ($p = ||, \perp$). For optical absorption measurements of protein crystals it is rarely possible to obtain the complete set of measurements because of the special requirements for well-developed crystal faces of optical quality perpendicular to each of the crystallographic

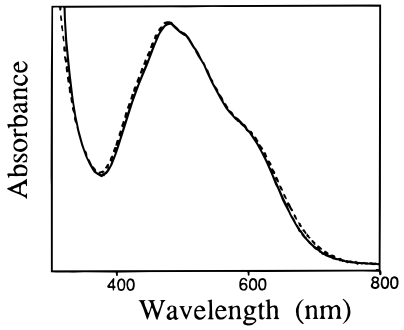


**Figure 8.** Comparison of crystal spectra and solution spectra: (- - -) averaged crystal spectra ($A_{||} + 2A_{\perp}$); (—) solution spectrum for *E. coli* Mn superoxide dismutase (2 mM active sites; 50 mM $KHPO_4$ buffer, pH 7).

directions allowing the light beam to enter at normal incidence. In the present case the crystal structure determined by X-ray diffraction studies implies similar polarization for spectra on the *ac* and *bc* faces and a spectrum resembling the perpendicular spectrum for *ac* justifying a simplified expression:

$$A_{b,||} + 2A_{b,\perp} \approx A_{\text{sol}} \tag{4}$$

This approximate equality is confirmed by the results in Figure 8, showing the polarization sum and the solution spectrum are nearly indistinguishable. This also supports the near equivalence of active site structures in solution and in the crystal. In this regard, it has been noted that PEG polymer used for crystallization does not penetrate into protein crystals, and therefore the solvent environment of the proteins in the lattice is essentially the same as in solution.[35]

The projection of the crystallographic *c*-axis onto the four independent Mn sites of the asymmetric unit is shown in Figure 5 (lower right). For all four sites, the *c*-axis (the predominant axis for polarization of the second ligand field band) is roughly aligned with the Mn−carboxylate bond but rotated relative to the Mn−O(carboxylate) vector in the equatorial ligand plane by approximately 40° and raised 5°−25° out of the plane. Since the experimental polarization has a small perpendicular component for the second ligand field band, the *c*-axis is not necessarily an exact polarization axis. However, a close alignment of crystallographic and transition moment vectors is indicated by the large polarization ratio (Table 1), suggesting a projection of at least 90% for the transition dipole moment on the crystallographic axis. The orientation of this axis corresponds closely to the transition moment predicted for carboxylate-to-Mn(III) LMCT (see above) in computational experiments. The polarization vector approximately bisects the carboxylate group as predicted in DFT calculations on the model structure.

The identification of significant carboxylate CT character in this absorption is important for interpretation of the optical spectra of MnSOD complexes and understanding the properties of the electronic ground state. The intense ligand field

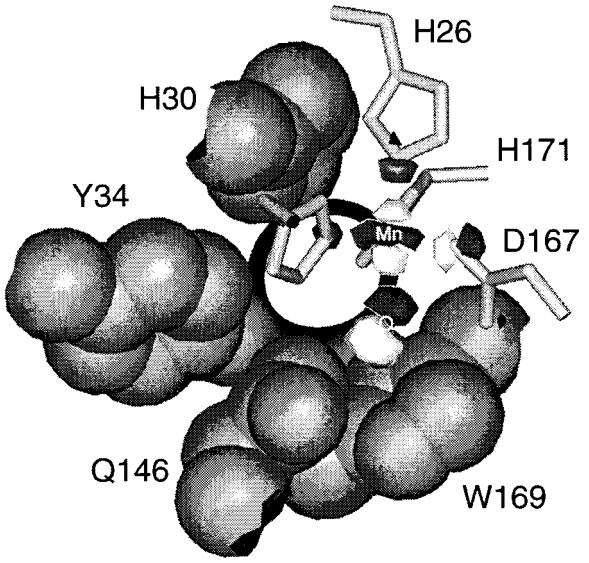


**Figure 9.** Redox orbital for Mn(III) superoxide dismutase superimposed on the active site. View from the interior of the protein through the base of the substrate/solvent funnel, marked by the circle in the figure. Directly coordinated metal ligands are shown in stick representation, while outer-sphere residues are depicted in CPK space-filling view. The positions of the Mn ion and the solvent (OH) ligand are labeled. The redox orbital is represented as an electron amplitude isosurface contoured at 0.05 e/Å$^3$.

absorption for the Mn(III) in the protein has previously been variously attributed to interactions with the solvent, histidine imidazoles, or aspartic carboxylate. The present spectroscopic studies give firm experimental and theoretical basis for assignment of the origin of this intense absorption to covalent mixing with the carboxylate ligand. Carboxylate mixing in the Mn(III) ground state will tend to stabilize the oxidized complex through a ground-state CT mechanism that delocalizes the redox orbital over the metal ligands.[19] The characteristic decrease in absorption on binding exogenous anions to the Mn(III) center of MnSOD is associated with a decrease in absorption in the lowest energy LF bands without significant shifts in CD bands. The differential absorption between native and anion complexes peaks near 500 nm and closely resembles the *c*-polarized crystal spectrum (Figure 3), consistent with a decrease in Mn−carboxylate interactions in the anion complex. This supports our previous proposal of carboxylate lability based on spectroscopic data and crystallographic results for *Thermus thermophilus* MnSOD−azide complexes,[36] suggesting a stretch of the Mn−O(carboxylate) vector on binding azide.

The patterns of orbital splittings computed by molecular orbital calculations on the Mn(III) complex are quite similar to the patterns of d-orbital splittings predicted by qualitative ligand field theory.[14,33,34] For high-spin Mn(III), the five metal 3d orbitals are occupied by four electrons with parallel spin. In distorted trigonal geometry, the ground state is mainly $d_{z^2}$ in character. This unoccupied orbital defines the orbital symmetry of the many-electron ground state for the $d^4$ metal ion and is the redox orbital of the complex. The strong $\sigma$ overlaps between $d_{z^2}$ and the coordinated solvent emphasize the importance of this ligand for the redox properties of the complex. Ligand interactions will be important for tuning the binding energy of the redox orbital and so controlling redox properties of the complex and may also contribute an outer-sphere electron-transfer pathway into the active site. Superposition of the ground-state redox orbital onto the protein structure (Figure 9) illustrates how hydroxide contributions to the redox orbital extend the orbital into the base of the substrate funnel, thus facilitating electron transfer to the Mn center from redox-active molecules in the funnel.

Reduction of the Mn(III) center is coupled to protonation of the coordinated solvent in catalysis.[16] Calculations of the ground-state geometry and electronic structure for reduced (model **B**) and protonated (model **C**) complexes have allowed us to investigate these events in the context of a DFT analysis. The dramatic change in metal−ligand covalency between Mn(III) and Mn(II) forms (Tables 1−3) is an important aspect of redox reactivity in this complex. Interactions with the coordinated oxygens appears to be especially important, making contributions that stabilize the Mn(III) complex.[19] The Mn−O(solvent) vector undergoes a significant elongation when the metal is reduced (Figure 7) and is the single largest metric change in the structure associated with redox chemistry in the complex. The driving force for this distortion can be traced to $\sigma$ antibonding interactions between Mn and the ligated solvent, which are fully expressed when the metal $d_{z^2}$ redox orbital is populated in the reduced complex. Since the position of the coordinated solvent is relatively unconstrained in the protein, this Mn−O(solvent) stretch will represent a significant coordinate coupled to electron-transfer reactions of the active site. As a result of this distortion, the experimental Mn−O distance for MnSOD obtained by X-ray crystallography can be expected to be sensitive to partial reduction of the Mn centers during crystallization or data collection (see above). Protonation of the solvent produces further distortions of the molecular geometry, including additional Mn−O elongation and a dihedral twist for the equatorial imidazole adjacent to the second protonation site on the coordinated solvent in the aquo complex (**C**). The steric interactions that lead to this twist will also be present in the biological active site and may account for a relatively large dihedral angle for one of the two equatorially coordinated histidine imidazoles (H171) as a conserved feature of superoxide dismutase structure (Figure 1).[10] The possibility that this identifies a special proton binding site on the coordinated solvent is supported by the observation that the alternative solvent protonation site is engaged as an acceptor for a hydrogen bond with a glutamine residue (Q146) in the protein.[10]

## Conclusions

Mn(III)−carboxylate LMCT is an important intensity component of the excited-state spectra for Mn(III)SOD, reflecting significant covalency of the metal−ligand interactions. Together, hydroxide and carboxylate ligand contributions are expected to dominate the chemistry of this active site. Mn−carboxylate covalency leads to significant electron delocalization in the ground state (representing as much as 0.8 e charge donation into the valence shell of the Mn(III) metal complex) and is thus likely to be important for redox tuning of this active site. The evidence for weakening of the carboxylate−Mn(III) interactions in MnSOD anion adducts suggests that the carboxylate group also contributes to (de)stabilizing complexes including the peroxyanion product complex of the turnover reaction. Hydroxide contributions to the Mn(III) ground state are important for coupling protons with redox chemistry. The redox orbital is extended into the base of the substrate funnel at the gateway of the active site by delocalization over the hydroxide ligand, which may serve as an effective pathway for outer-sphere redox in the Mn(III) complex as well as for transfer of an electron from Mn(II)SOD to an incoming superoxide anion. A significant stretch in the Mn−OH(H) coordinate is

predicted to be associated with metal redox and is expected to play an important role in the chemistry of this complex.

## References and Notes

(1) Fridovich, I. *Adv. Enzymol.* **1986**, *58*, 61−97.
(2) Fridovich, I. *Annu. Rev. Biochem.* **1995**, *64*, 97−112.
(3) Bannister, J. V.; Bannister, W. H.; Rotilio, G. *CRC Crit. Rev. Biochem.* **1987**, *22*, 111−80.
(4) Keele, Jr., B. B.; McCord, J. M.; Fridovich, I. *J. Biol. Chem.* **1970**, *245*, 6176−6181.
(5) Weisiger, R. A.; Fridovich, I. *J. Biol. Chem.* **1973**, *248*, 4793−4796.
(6) Yost, F. J., Jr.; Fridovich, I. *J. Biol. Chem.* **1976**, *251*, 4905−4908.
(7) McCord, J. M.; Fridovich, I. *J. Biol. Chem.* **1969**, *244*, 6049−6055.
(8) Youn, H.-D.; Kim, E.-J.; Roe, J.-H.; Hah, Y. C.; Kang, S.-O. *Biochem. J.* **1996**, *318*, 889−96.
(9) Ludwig, M. L.; Metzger, A. L.; Pattridge, K. A.; Stallings, W. C. *J. Mol. Biol.* **1991**, *219*, 335−58.
(10) Edwards, R. A.; Baker, H. M.; Jameson, G. B.; Whittaker, M. M.; Whittaker, J. W.; Baker, E. N. *J. Biol. Inorg. Chem.* **1998**, *3*, 161−171.
(11) Borgstahl, G. E.; Parge, H. E.; Hickey, M. J.; Beyer, W. F., Jr.; Hallewell, R. A.; Tainer, J. A. *Cell* **1992**, *71*, 107−18.
(12) Gray, H. B.; Winkler, J. R. *Annu. Rev. Biochem.* **1996**, *65*, 537−561.
(13) Thomson, A. J.; Breton, J.; George, S. J.; Butt, J. N.; Armstrong, F. A.; Hatchikian, E. C. *Biochem. Soc. Trans.* **1991**, *19*, 594−599.
(14) Whittaker, J. W.; Whittaker, M. M. *J. Am. Chem. Soc.* **1991**, *113*, 5528−40.
(15) Whittaker, M. M.; Whittaker, J. W. *Biochemistry* **1996**, *35*, 6762−70.
(16) Bull, C.; Niederhoffer, E. C.; Yoshida, T.; Fee, J. A. *J. Am. Chem. Soc.* **1991**, *113*, 4069−76.
(17) Bjerrum, M. J. *Biochim. Biophys. Acta* **1987**, *915*, 225−237.
(18) Whittaker, J. W. *J. Phys. Chem. B* **1997**, *101*, 674−677.
(19) Fisher, C. L.; Chen, J.-L.; Li, J.; Bashford, D.; Noodleman, L. *J. Phys. Chem.* **1996**, *100*, 13498−13505.
(20) Touati, D. *J. Bacteriol.* **1983**, *155*, 1078−1087.
(21) Beem, K. M.; Richardson, J. S.; Richardson, D. C. *J. Mol. Biol.* **1976**, *105*, 327−332.
(22) Lowry, O. H.; Rosebrough, N. J.; Farr, A. L.; Randall, R. J. *J. Biol. Chem.* **1951**, *193*, 265−275.
(23) Beyer, W. F.; Reynolds, J. A.; Fridovich, I. *Biochemistry* **1989**, *28*, 4403−4409.
(24) Hedin, L.; Lundquist, B. I. *J. Phys. C* **1971**, *4*, 2064−2083.
(25) Becke, A. D. *J. Chem. Phys.* **1988**, *88*, 2547.
(26) Perdew, J. P.; Wang, Y. *Phys. Rev.* **1992**, *B45*, 13244.
(27) Pulay, P. *J. Comput. Chem.* **1982**, *3*, 556.
(28) Pulay, P. *Chem. Phys. Lett.* **1980**, *73*, 393.
(29) Bloss, F. D. *An Introduction to the Methods of Optical Crystallography*; Holt, Rinehart and Winston: San Francisco, 1961.
(30) Hitchman, M. A. *Transition Met. Chem.* **1985**, *9*, 1−93.
(31) Shirin, Z.; Young, V. G., Jr.; Borovick, A. S. *Chem. Commun.* **1997**, 1967−1968.
(32) Slater, J. C. *Adv. Quantum Chem.* **1972**, *6*, 1−92.
(33) Ballhausen, C. J. *Introduction to Ligand Field Theory*; McGraw-Hill: San Francisco, 1962.
(34) Griffith, J. S. *Theory of Transition-Metal Ions*; Cambridge University Press: Cambridge, 1964.
(35) Eichele, G.; Karabelnik, D.; Halonbrenner, R.; Jansonnius, J. N.; Christen, P. *J. Biol. Chem.* **1978**, *253*, 5239−5242.
(36) Lah, M. S.; Dixon, M. M.; Pattridge, K. A.; Stallings, W. C.; Fee, J. A.; Ludwig, M. L. *Biochemistry* **1995**, *34*, 1646−60.